Multifractal detrended fluctuation analysis of photon intensity time series in solvent-filled nano-structured porous media

by

Luqman Opeyemi Olawale

B.S., Osun State University, 2016

A THESIS

submitted in partial fulfillment of the requirements for the degree

MASTER OF SCIENCE

Department of Geology
College of Arts and Sciences

KANSAS STATE UNIVERSITY
Manhattan, Kansas

2024

Approved by:

Co-Major Professor
Dr. Daniel A. Higgins

Approved by:

Co-Major Professor
Dr. Behzad Ghanbarian

Copyright

Abstract

Single molecule fluorescence fluctuation experiments were conducted to uncover complex molecular mass transport dynamics in nanoporous media. Confocal fluorescence microscopy was employed to capture single-molecule photon intensity time series from bulk solution and from porous anodic aluminum oxide (AAO) membranes incorporating 10 and 20 nm diameter pores. The membranes were filled by 20 nM Nile red (NR) dye solution in pure ethanol and pure toluene. Regardless of the solvent, the photon intensity time series revealed clear evidence of dye diffusion along the one-dimensional nanopores, as well as evidence of dye adsorption to the pore surface in the 10 nm membranes. Autocorrelation of the time series revealed that NR diffused through the 10 nm membrane by two distinct mechanisms that could be classified as fast and slow diffusion. The diffusion coefficients, D_f and D_s, yielded values differing by 100-fold. The fast mechanism was attributed to hindered bulk-like diffusion in the central pore cavity, while slow diffusion likely involved absorption and desorption of the dye at the pore surface. Interestingly, only fast diffusion was observed in the 20 nm membrane. While autocorrelation functions frequently reveal the occurrence of multicomponent diffusion, it can be challenging to distinguish Fickian and anomalous diffusion mechanisms. The method of multifractal detrended fluctuation analysis (MF-DFA) from statistical physics was applied to the photon intensity time series as a means to further characterize the diffusion mechanisms. The MF-DFA analysis afforded values for the generalized Hurst exponent, $h(q)$, of ~ 0.5 for times series obtained from bulk solution, consistent with Fickian diffusion. For both the 10 and 20 nm membranes, $h(q) > 0.5$ was obtained, consistent with super diffusion. Application of MF-DFA methods to photon times series affords additional evidence needed to better characterize the mechanisms of molecular transport in nanoporous media such as in oil and gas shales.

Table of Contents

List of Figures

List of Tables

Acknowledgements

I humbly offer my deepest gratitude to Almighty Allah for guiding me along this remarkable journey and for bestowing upon me the strength, wisdom, and perseverance necessary to navigate through the challenges and triumphs of completing this thesis.

I owe a great debt of gratitude to my respected academic advisors, Dr. Behzad Ghanbarian and Dr. Daniel Higgins. Their wise counsel, mentorship, and constant encouragement have played a crucial role in directing the path of my research efforts. Their knowledge, commitment, and scholarly perspectives have greatly enhanced this study, and I am incredibly thankful for their priceless contributions.

Furthermore, I express my sincere appreciation to my esteemed advisory committee member, Dr. Matthew Brueseke, whose expertise have been indispensable in shaping this research.

A special word of gratitude is extended to Omid Shafiee for his invaluable assistance and unwavering support throughout every phase of this research endeavor, from the initial stages of conceptualization to the meticulous execution of laboratory experiments and data analysis. His dedication and expertise have been instrumental in advancing this study to fruition. Also, I am deeply grateful to my friends and colleagues who have offered unwavering support, and encouragement throughout this journey.

I also wish to express my profound appreciation to the funding agencies that have generously supported this research endeavor, including the American Chemical Society Petroleum Research Fund, Department of Geology Kansas State University, the Kansas Geologic Foundation, the American Geophysical Union, and the K-State Graduate School. Their financial support and recognition have been integral to the successful completion of this study.

Lastly, I extend my heartfelt gratitude to Kansas State University for providing an enriching academic atmosphere that fosters cerebral research pursuits. The university's commitment to excellence in education and research has provided me with invaluable opportunities for intellectual growth and development.

Dedication

I dedicate this thesis to my beloved mother, whose unwavering love and endless encouragement guided me through every step of my life journey. Though you're no longer with us in person, your spirit and influence continue to shape my life and aspirations. Your memory fuels my determination, and I dedicate this thesis to you with profound gratitude and love.

To my cherished spouse, whose boundless patience, support, and understanding have been my constant companions throughout this endeavor. Your unwavering belief in me has been a source of strength and inspiration. Thank you for standing by me through every challenge and triumph.

Chapter 1 - Introduction

Unconventional reservoirs including oil and gas-bearing shales are distributed around the world and have an estimated endowment of several thousand trillion cubic feet of carbon (Ghanbarian et al., 2023). Tight and ultra-tight reservoirs are now being successfully produced and represent key contributors to energy supplies. Despite recent advances, our understanding of fluids flow and transport mechanisms in unconventional reservoirs remains incomplete. Morphology, pore structure, and heterogeneity of mudrocks are important because they affect oil and gas transport in the network of nano- and micro-scale pores and microfractures (Loucks & Reed, 2014) and inorganic matrices (Loucks et al., 2012).

Full production of unconventional reservoirs is limited in part by the incomplete understanding of mass transport mechanisms at the molecular level within nanostructured shales. Although molecular dynamics simulations (Castez et al., 2017; Fang et al., 2017; He et al., 2020; Huang et al., 2018; Ungerer et al., 2015; Zhang et al., 2020) have provided valuable insights, experimental data on diffusion dynamics at the molecular-level in nanoporous media is lacking. The transport rate of oil and gas is controlled by partitioning between different phases and by the viscosity of fluid filling the pores. Interfacial adsorption is also certain to be important, due to the high interface-to-volume ratio and the potential for both chemical and physical interactions between individual molecules and the pore surfaces. Such interactions frequently impede oil and gas diffusion. A better understanding of the mechanisms of diffusion in nanoporous materials is certain to aid in oil and gas production from these reservoirs. More specifically, it is well documented that production rate decreases after a few months of hydrocarbon extraction in unconventional reservoirs (Hakso & Zoback, 2019). This is mainly due to pressure drop in subsurface and change in transport mechanisms from advection-type (hydraulic fracturing) to

diffusion. Therefore, decoding mass transport mechanisms at the molecular level is essential and in combination with appropriate upscaling techniques helps improve production at reservoir scales.

Mass transport within nanostructured media has been studied extensively by ensemble methods that primarily report on the average behavior of a large number of molecules (Cussler, 1997). For example, flux methods are based on monitoring the concentration of permeants and provide insights into the mass transport processes. However, they do not allow for molecular motions to be explicitly visualized, nor can molecule-matrix interactions be directly detected. Optical methods, such as fluorescence recovery after photobleaching, have been employed to study mass transport rates and anisotropies in nanostructured materials (Tran-Ba et al., 2015). The dynamics of mass transport has also been studied by quasi-elastic neutron scattering (Takahara et al., 2008), while longer (microsecond-second) motions have been probed by dielectric spectroscopy (Takahara et al., 2008; Vinh et al., 2011). Nuclear magnetic resonance spectroscopy has also been applied to study mass transport rates and anisotropies (Cho et al., 2012; Kärger & Valiullin, 2013). All such methods suffer from extensive signal averaging across large numbers of pores and molecules. With the advent of optical single-molecule detection methods (Brooks Shera et al., 1990; Eigen & Rigler, 1994; Moerner & Kador, 1989; Orrit & Bernard, 1990), it has become feasible to detect the motions of individual fluorescent molecules within individual pores.

In Figure 1, we show the nano-CT image of a shale sample as well as the corresponding pore size distribution with pore size ranged from 5 to 12 nm. Therefore, in this study, mass transport phenomena are probed within solvent-filled nanoporous anodic aluminum oxide (AAO) membranes. The AAO membranes serve as a model for nanoporous shales. Fluorescence-based confocal optical single molecule detection methods are leveraged to detect and probe diffusion at the single molecule level. In this study, ethanol and toluene are used as solvents to mimic

hydrocarbons while nile red dye was used as hydrocarbon tracer. This choice is further supported by contact angle measurements, indicating similarities between the solvents' interactions with shale and membrane surfaces (details of this analysis are not presented here).

Photon intensity time series recorded on the confocal microscope reveal bursts of fluorescence arising from diffusion of NR through the detection volume and its adsorption and desorption from pore surfaces. Initial analysis of the time series data is accomplished by autocorrelation methods, which afford measures of the diffusion coefficient and initial information on the diffusion mechanism. Additional knowledge of the diffusion mechanism is obtained by applying the method of multifractal detrended fluctuation analysis (MF-DFA) in further analysis of the photon intensity series data. It is shown that by quantifying the scaling behavior of fluctuations across different time scales, MF-DFA can provide additional insights into the underlying dynamics that may not be readily apparent based on traditional fluorescence correlation spectroscopy (FCS) analysis (Elson & Magde, 1974).

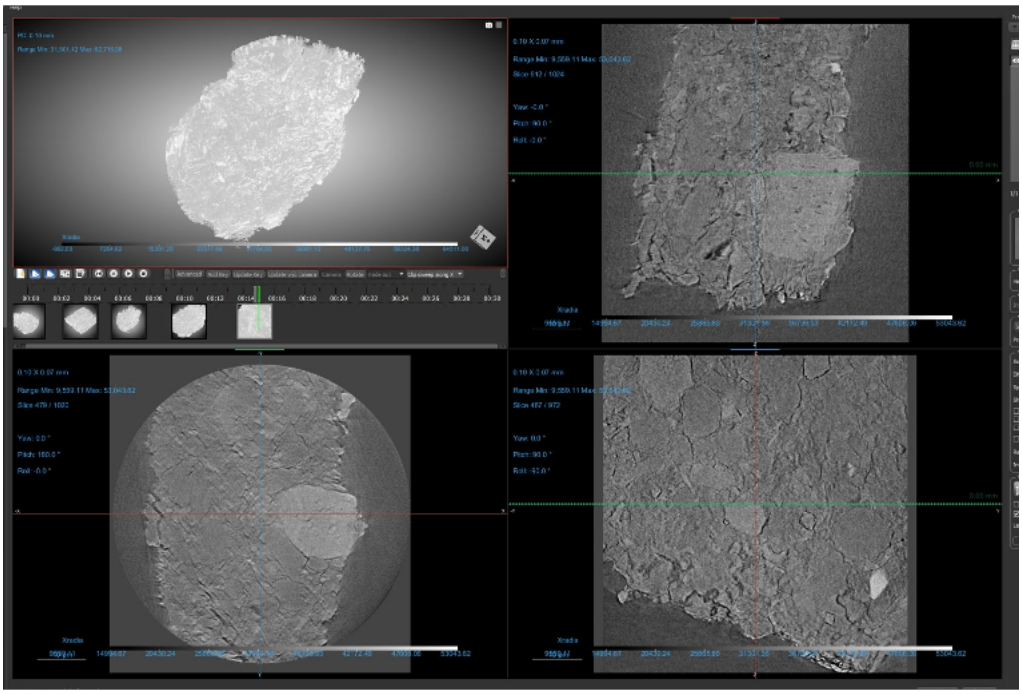

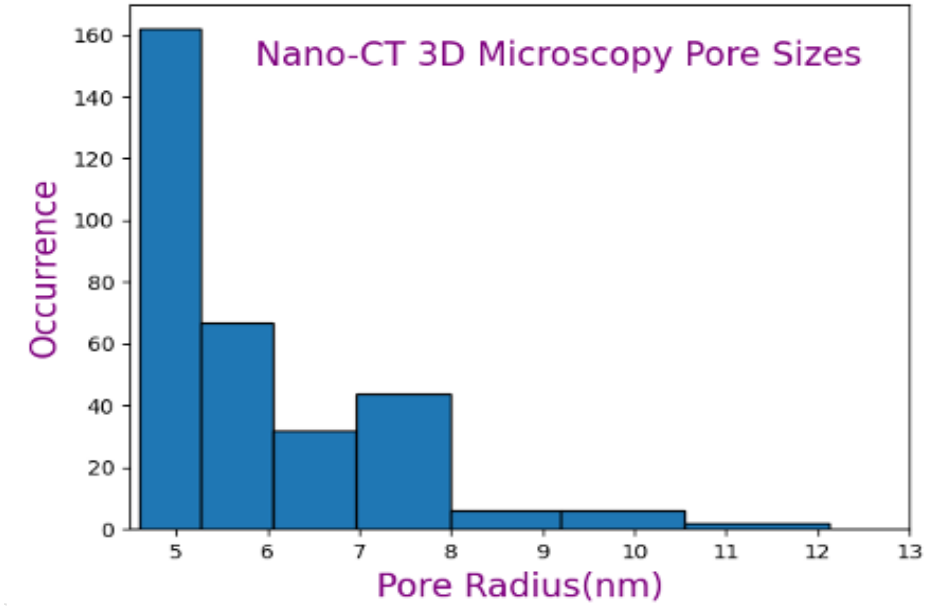

Figure 1.1 Nano-CT X-ray imaging of shale at the top and the pore size distribution with pores ranged from 5 to 12nm with average pore radius of 6nm at the bottom.

Chapter 2 - Fluorescence Correlation Spectroscopy

Fluorescence Correlation Spectroscopy (FCS) has emerged as one of the powerful tools for probing the dynamics of biomolecules and nanoparticles with unprecedented precision and sensitivity. This technique offers unique insights into the spatiotemporal behavior of molecules in solution, enabling researchers to unravel complex molecular interactions and dynamics at the single-molecule level. The concept of Fluorescence Correlation Spectroscopy (FCS) originated in 1972 through the pioneering work of (Magde et al., 1972). It was first utilized to investigate the diffusion and chemical dynamics of DNA-drug intercalation, FCS has since been adopted by numerous researchers to examine particle concentration and molecular dynamics in both two and three dimensions.

FCS single-molecule investigations revolve around the detection and tracking of individual fluorescent dye molecules' movements. These techniques have found widespread application in exploring mass transport within nanoporous media (Hohlbein et al., 2007; Higgins et al., 2015; Rashidi et al., 2023). By employing single-molecule measurements, the extensive signal averaging of ensemble methods is avoided, enabling the differentiation of individual transport processes. Also, utilizing single-point photon time series-based fluorescence correlation spectroscopy (FCS) (Aragón et al., 1976; Brooks Shera et al., 1990) allows for the quantitative assessment of local concentrations, molecular diffusion coefficients, adsorption, and desorption times, as well as the confinement of molecular motions.

2.1 Materials

Nile red (NR) fluorescence dye used in this study was bought from the Sigma- Aldrich and was used as received. The decision to employ NR dye for this research stemmed from its

robust fluorescence characteristics, enabling highly sensitive detection in experimental settings. Additionally, its molecular size is smaller than the pores within the nanoporous structure, enabling efficient diffusion through the pores. The dye's chemical stability also ensures the reliability of fluorescence signals throughout the experiment, while its minimal photobleaching allows for their prolonged observation. The concentration of NR was maintained at 20 nanomolar (nM) in all the confocal single-point experiments. Pure toluene and pure ethanol were obtained from Fisher chemical (HPLC grade) and Decon laboratories Inc respectively and were used as received. These were used as proxies for natural hydrocarbon in place.

Nanoporous anodic aluminum oxide (AAO) membranes composed of cylindrical pores of diameter 10±3 and 20±3 nm were procured from InRedox LLC (Figure 2.1). The membranes were obtained as 10±0.1 mm wafer disks with cylindrical pores extending across the full 50±2 μm membrane thickness. The porosity of the membranes was reported by the supplier as 12±2%. The membranes were subsequently cut into smaller chips prior to use. To ensure the pores were filled with the desired solvent, each chip of the membranes was first immersed in either pure toluene or pure ethanol for at least one day. At the start of each experiment, the membranes were transferred to a sample cell, which consisted of a hollow cylinder glued to a thin cover glass for mounting on the microscope and were immediately immersed in one of the NR solutions.

(a)

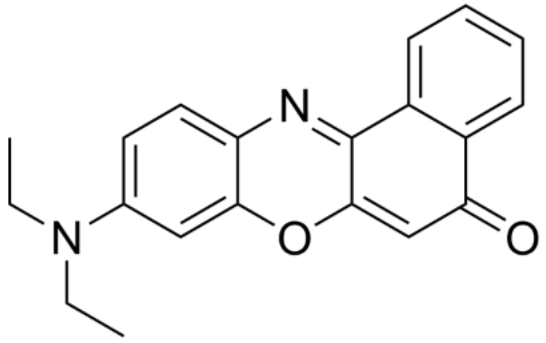

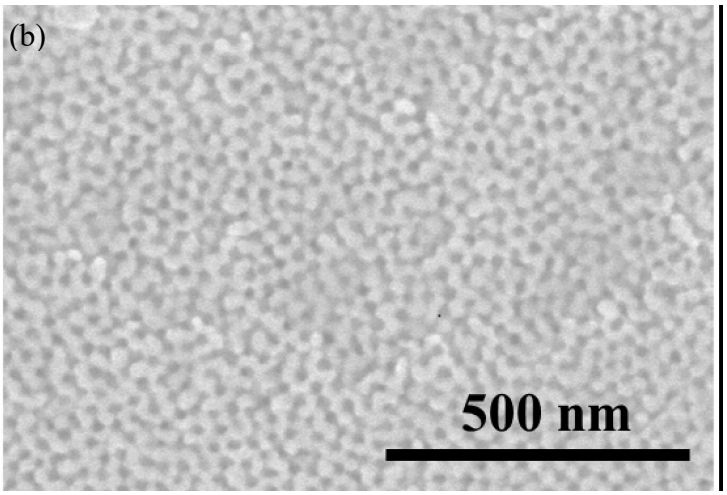

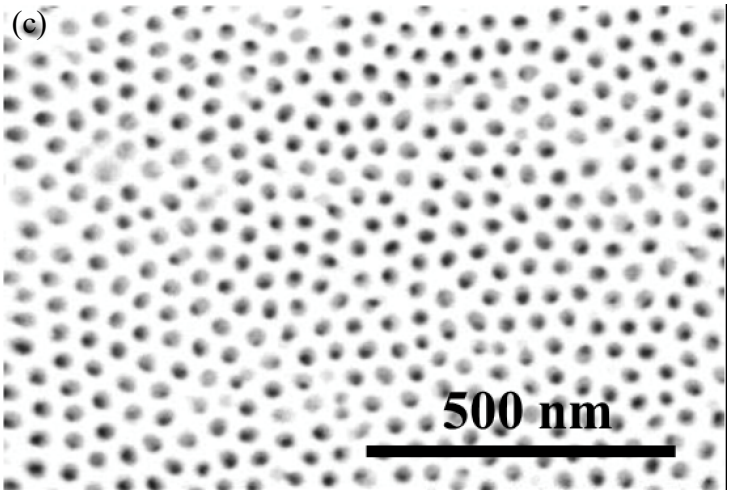

Figure 2.1 (a) Chemical structure of Nile red dye, (b and c) scanning electron microscopy (SEM) images of 10 and 20nm AAO membrane respectively (Rashidi et al., 2023).

2.2 Measurements

Fluorescence correlation spectroscopy (FCS) experiments were conducted on a custom-built confocal fluorescence optical microscope, utilizing a commercial inverted light microscope as the foundation (refer to Figure 2.2a.). The system was designed for capturing single-point fluorescence photon time series. A 532nm wavelength solid-state laser served as the excitation source for the fluorescence of single-molecule Nile red (NR) dye. Initially, the laser light passed through two lenses serving as a telescope. There allow for control of the beam diameter and its divergence. The laser light passes through halfwave-plate polarizer combination in order to set the laser power delivered to the microscope. The light is then directed onto a dichroic mirror (beamsplitter). An incident power of 5μW, measured prior to incidence on the dichroic beam splitter, was used in all experiments. The dichroic mirror selectively reflects or transmits light based on its wavelength. It reflects the green light from the laser into the aperture of the high numerical oil immersion objective lens, the objective focusses the laser into the sample exciting the nile red dye. The immersion oil has a refractive index closely matched to that of the glass and the specimen. The immersion oil is employed to enhance the numerical aperture (NA) and collection efficiency of the objective lens, and to achieve a tighter laser focus and smaller detection volume.

Fluorescence emitted from the sample is collected utilizing the same objective lens. The collected light is redirected back through the dichroic mirror and focused through a suitably sized pinhole positioned in the image plane of the microscope. The pinhole blocks out-of-focus light from reaching the detector by allowing only light from focal plane to pass through. The light eventually traverses a bandpass emission filter before being imaged onto the detector. A single-photon-counting avalanche photodiode (APD) was used in these studies.

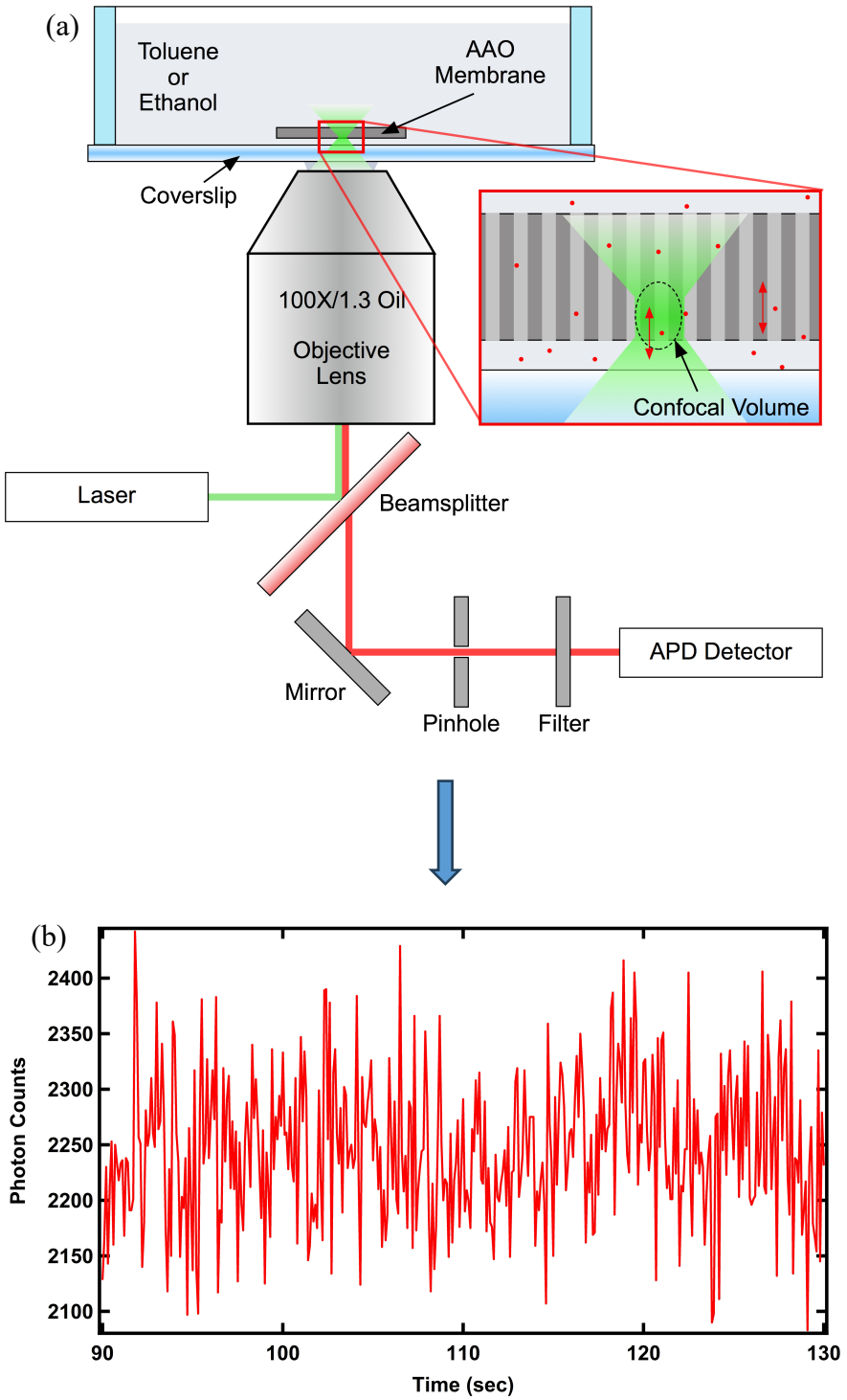

Figure 2.2: (a) Experimental setup employed in FCS experiments for recording time transient data (courtesy of Dr. Daniel Higgins), (b) Typical illustration of a photon intensity transient.

This setup enabled the recording of fluorescence photon time series from femtoliter volumes across microsecond and longer timescales. The electrical pulses captured by the APD are time tagged/ or stamped and stored as a 32-bit unsigned binary integer. The data are autocorrelated and analyzed using a C++ code written in-house. Simultaneously, a Python script developed in-house performs byte-swapping on the 32-bit unsigned integer data. This byte-swapping process generates arrays representing photon intensity. Following this, photon intensity time series with bin times of 0.1, 1, and 10 ms time transient are extracted from these arrays. These extracted datasets are then utilized for Multifractal Detrended Fluctuation Analysis (MFDFA) to delve deeper into the nature of the diffusion mechanism.

2.3 Autocorrelation Analysis

The photon intensity time series (see Figure 2.2b) are then autocorrelated using equation (1). The autocorrelation function enables the examination of time-dependent intensity fluctuations, revealing molecular diffusion dynamics. Autocorrelating the time series offers quantitative insights into NR diffusion rates and mechanisms, enhancing understanding of underlying processes in FCS analysis.

$$G(\tau) = \frac{<F(t)F(t+\tau)>}{<F(t)>^2} - 1 \quad (1)$$

where $G(\tau)$ is the autocorrelation function, $F(t)$ represent the photon intensity time series, and $F(t+\tau)$ a copy of the time series delayed by time τ. The $<>$ denotes averaging over the time transient.

Chapter 3 - Multifractal Detrended Fluctuation Analysis

To interpret the photon intensity time series data recorded on the confocal fluorescence microscope and compare results of the bulk solution with those of AAO membranes and to further characterize the diffusion mechanisms the multifractal detrended fluctuation analysis (MF-DFA) was employed. The MF-DFA is an approach from statistical physics used to study multifractal and scaling properties of both stationary and nonstationary time series (Kantelhardt et al., 2002a; Peng et al., 1994). It was initially proposed by Peng et al. (1994) as a basic detrended fluctuation analysis and later extended by Kantelhardt et al. (2002a) to study multifractal processes. It is a versatile analytical tool that addresses the fundamental question of correlation presence in time series and can be employed to analyze both discrete as well as continuous-time stochastic processes. Multifractal time series analysis has a wide range of applications across various disciplines. For instance, it has been utilized to investigate complex phenomena in the field of healthcare (Dutta et al., 2013; Ihlen, 2012; Ivanov et al., 1999; Madanchi et al., 2020; Pavlov et al., 2020), seismic activity (Shadkhoo et al., 2009; Telesca et al., 2005), sunspot activity (Movahed et al., 2006), climate science (Morales Martínez et al., 2021; Pedron, 2010; Tessier et al., 1996), and geoscience (Alam et al., 2021; Mahale et al., 2022; Subhakar & Chandrasekhar, 2016).

Within the MF-DFA framework, one may calculate the profile series, $Y(i)$, from the original time series, $x(k)$, with length N as follows

$$Y(i) \equiv \sum_{k=1}^{i}[x(k) - \langle x \rangle], \quad \text{i} = 1, \ldots.\text{N}. \tag{2}$$

where $\langle x \rangle$ denotes the average of the $x(k)$ series. The profile series $Y(i)$ is then divided into N_s = int(N/s) non-overlapping segments of equal length s. One should note that the length of a time series may not necessarily be a multiple of the considered scale. Therefore, to consider any remaining, unused data at the end of the profile series one should repeat this process from the

opposite end, giving to total of $2N_s$ segments. For each segment, a polynomial function with some arbitrary degree (e.g., linear, quadratic, cubic, or higher order) is fit, and the variance function is determined for segments $v = 1, \dots, N_s$ as follows

$$F^2(s,v) = \frac{1}{s}\sum_{i=1}^{s}\{Y[(v-1)s+i] - y_v(i)\}^2 \quad (3)$$

For segments $v = N_s + 1, \dots, 2N_s$, however, the variance function is given by

$$F^2(s,v) = \frac{1}{s}\sum_{i=1}^{s}\{Y[i+N-(v-N_s)s+i] - y_v(i)\}^2\ \} \quad (4)$$

In equations (3) and (4), $y_v(i)$ represents the fitting polynomial in the segment v (Kantelhardt et al., 2002a).

Then, the q[th] order fluctuation function is calculated by averaging over all segments

$$F_q(s) = \{\frac{1}{2N_S}\sum_{v=1}^{2N_s}[F^2(s,v)]^{q/2}\}^{1/q} \quad (5)$$

for any real value of q except zero. Negative and positive q values correspond to frequent and rare events in the time series $x(k)$. By increasing the time scale s, the $F_q(s)$ increases as well. The double logarithmic plot of $F_q(s) - s$ data for each value of q is characterized by the following power law

$$F_q(s) \sim s^{h(q)} \quad (6)$$

where $h(q)$ is the generalized Hurst exponent. In this study, we considered q_{min} = -100 and q_{max} = 100 to capture more of the trend in the photon intensity series, following Chen et al. (2004). Furthermore, following Telesca et al. (2018), we restricted the scale $x(k)_{min} \leq s \leq N_s/10$ where $x(k)_{min}$ is the minimum value of the time series and N_s is the length of the time series. Kantelhardt (2012) stated that the result of MF-DFA statistically become unreliable for s values greater than one tenth of series length. For some photon intensity series with numerous zero values, the scale was adjusted to $x(k)_o \leq s \leq N_s/10$ in which $x(k)_o$ signifies the number of maximum

consecutive zeros observed in the series (Drożdż et al., 2019). This adjustment was made to accommodate the high occurrence of zero values. In the MF-DFA, we used the linear-order polynomial in the fitting procedure corresponding to MF-DFA1.

In general, a time series is called multifractal, if the $h(q)$ varies with q (Movahed et al., 2006) and monofractal $h(q)$ if is independent of q (Sadegh Movahed & Hermanis, 2008) For stationary series, the Hurst exponent $H = h(q = 2)$, while for non-stationary series $H = h(q = 2) - 1$. (Movahed et al., 2006) $0 < H < 0.5$ indicates anti-persistence, while $0.5 < H < 1$ represents persistence (Movahed et al., 2006).

The MF-DFA provides a framework to assess whether data show mono- or multi-fractal behavior. The source of multifractality can be detected if one shuffles and surrogates data and reanalyzes them with the MF-DFA. Shuffling randomizes the order of data, and, thus, long-range correlations are destroyed, while surrogating generates random datasets with the same spectral density and autocorrelation structure as in the original time series (Sadegh Movahed & Hermanis, 2008). Multifractality could be due to either heavy tails in the probability density function (PDF) of data, large-range correlations in data, or a combination of both. Multifractality due to heavy-tailed PDFs cannot be eliminated by shuffling (randomizing) a series. Therefore, to determine the source of multifractality, data may be shuffled (e.g., 100 times). To surrogate a time series, data may be transformed using the Fourier transformation and repeated 100 times. Since the long-range correlations are destroyed by shuffling, one should expect the generalized Hurst exponent for shuffle time series $h_{shuf}(q) = 0.5$, if multifractality only pertains to long-range correlations. The process of shuffling has no impact on the multifractality nature resulting from the heavy tails of PDF. When a time series is surrogated, correlations in the surrogated series remain unchanged, but its PDF changes to a Gaussian distribution. Heavy-tailed PDFs only will be responsible for

multifractality, if $h(q) = h_{shuf}(q)$ and generalized Hurst exponent for surrogated series $h_{sur}(q) = 0$. On the other hand, deviations from $h_{sur}(q) = 0$ indicate the presence of correlation, and q dependence of $h_{sur}(q)$ indicates that multifractality is due to the long-range correlation. If both types of multifractality exists in a series, the shuffled series would show weaker multifractality than the original one.

To investigate the effect of time series length on the MF-DFA results, we performed a sensitivity analysis. We randomly generated photon intensity series based on the Poisson distribution using the NumPy Python library. The mean (or variance) of the Poisson distribution was determined from the pure ethanol experiments and set qual to 2.3, 23.0 and 229.6 for the 0.1, 1 and 10ms time bins. More specifically, three randomly generated series consistent with photon intensity datasets 0.1ms and length N_s = 1,500,000, 1ms and length N_s = 150,000, and 10ms and length N_s = 15,000 were analyzed (see Figure 3.1). The minimum and maximum photon counts were selected based on the experimental data collected in this study.

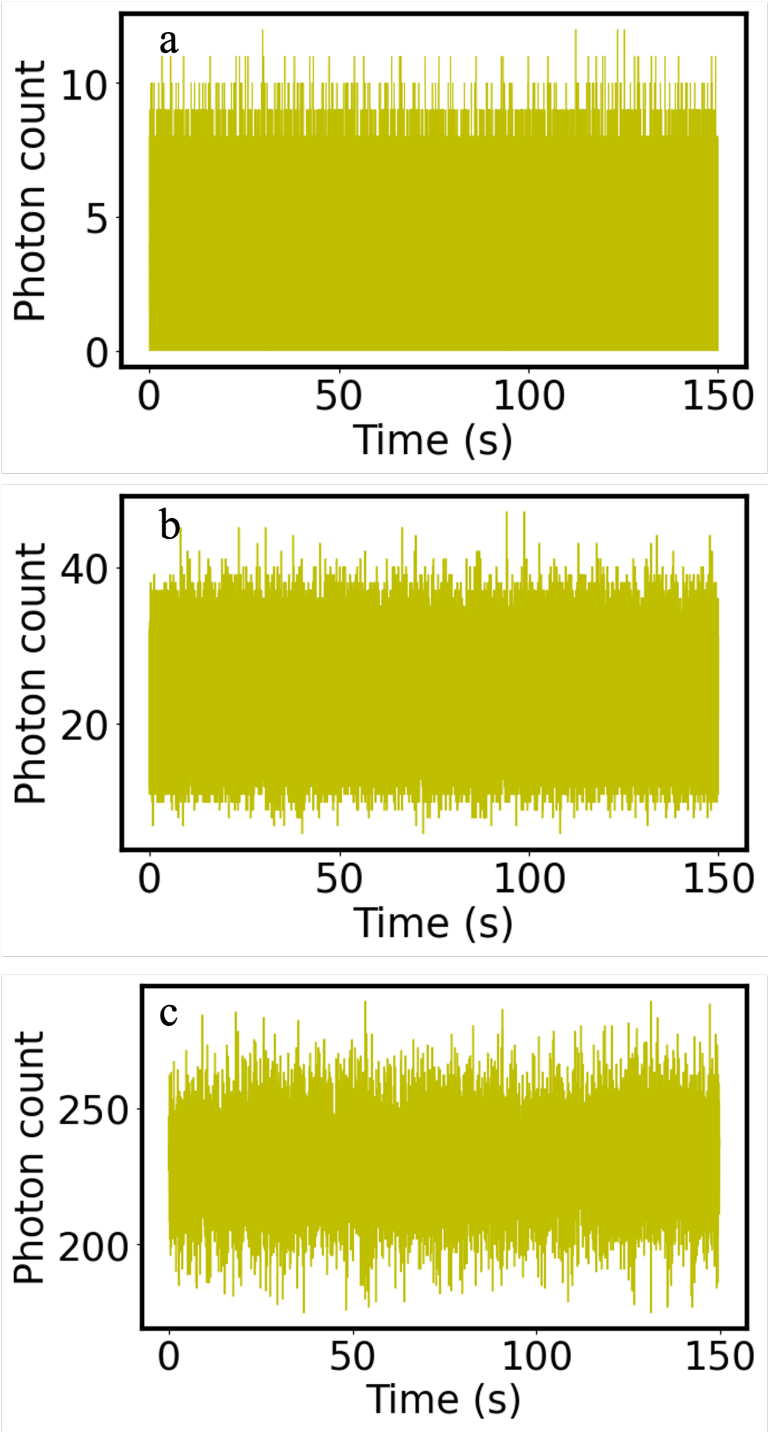

Figure 3.1 Randomly generated Time series of N_s =1,500,000, 150,000 and 15,000 data points following Poisson distribution. Poisson distribution was determined from the pure ethanol experiments and set equal to 2.3, 23.0 and 229.6 for the (a) 0.1, (b) 1 and (c) 10ms time bins.

Chapter 4 - Results and Discussion

4.1 Photon Intensity Time Transient

We first investigated the behavior of single molecular diffusion of NR molecules in the bulk solutions of pure ethanol and pure toluene as well as within confined solvent-filled AAO membranes by capturing photon intensity. Each transit event of individual dye molecules passing through the microscope focus generated a brief fluctuation in the fluorescence intensity. Figures 4.1a and 4.1c shows photon intensity time series for the NR in the bulk solution of pure ethanol and pure toluene, respectively, with noticeable increases in photon intensity observed when individual fluorescent molecules pass through the detection volume. The photon fluctuations arising from NR diffusion in the bulk solutions (Figure 4.1) manifest at a rate significantly faster than what can be adequately captured with 1ms bin times. Conversely, photon fluctuations identified within 10 and 20nm AAO membranes exhibit greater prominence, appearing less frequently and persisting for longer durations, which aligns with slower diffusion expected for NR with nanopores.

The photon fluctuations illustrated in Figures 4.1, 4.2 and 4.3 are different due to multiple factors. One possible explanation is molecular confinement within nanopores, which alters the diffusion dynamics of fluorescent molecules compared to those in the bulk solution. Additionally, interactions with pore surfaces can affect molecule mobility and fluorescence properties. Fluctuations in photon intensity may also arise from density variations of fluorescent molecules within nanopores, influenced by processes such as adsorption, desorption, or other surface interactions. Non-uniform excitation intensity across the confocal volume, particularly near pore entrances, can result in spatial variations in the fluorescence intensity. Directly visualizing fluorescence fluctuations from single molecule transit events could provide some basic idea of

diffusion mechanism. However, relying solely on this method is insufficient. Therefore, a more comprehensive approach i.e., the FCS autocorrelation is needed to address the diffusion mechanisms effectively.

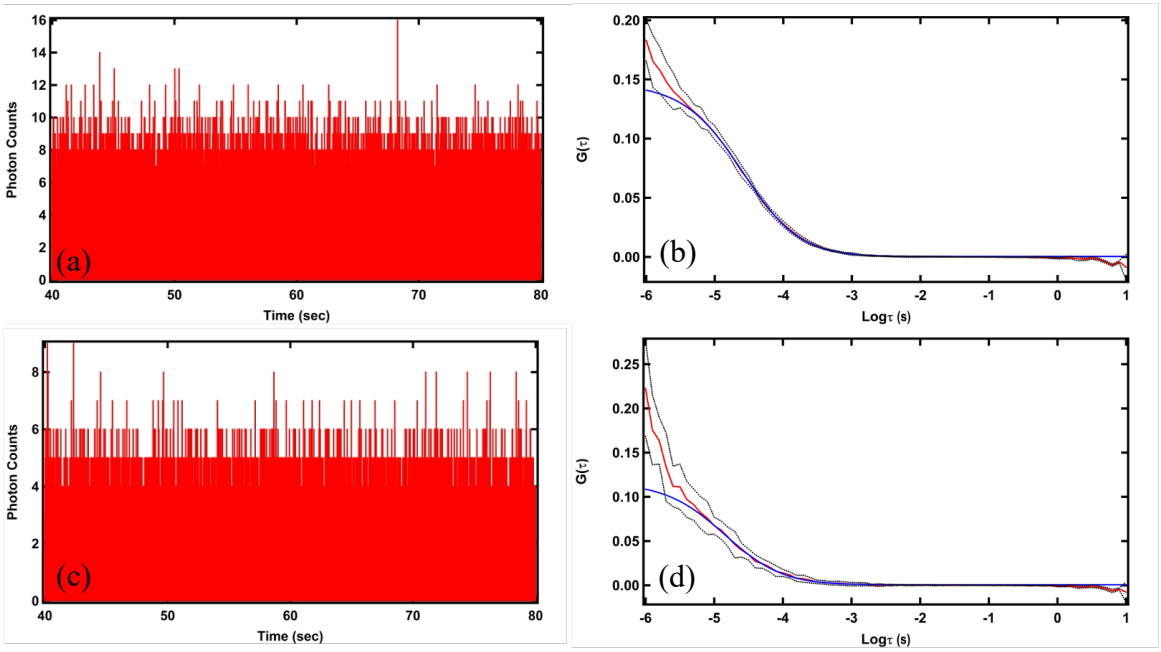

Figure 4.1 ((a , b) photons intensity series alongside its autocorrelation decay plot of NR in bulk ethanol solution, and (c, d) photons intensity series alongside its autocorrelation decay plot of NR in bulk toluene solution. The red line represents the autocorrelation function, the blue line represents the fitted model. The dash black line represents the 95% confidence interval.

4.2 Fluorescence Correlation Spectroscopy

Autocorrelation decays obtained from the fluorescence photon intensity time series offer quantitative insights into the rate of NR dye diffusion, while also unraveling evidence of the underlying diffusion mechanism. Utilizing equation (1), autocorrelation analysis was performed on all time transients.

Figures 4.1b and 4.1d show the autocorrelation decays for the bulk solutions of pure ethanol and toluene, respectively. The autocorrelation functions were fitted to a model for the decay expected from a 3D diffusion mechanism in bulk solution known as 3D one-component model.

$$\mathrm{G}(\tau) = A + \frac{1}{N}\left[\frac{1}{\left(\frac{\tau}{\tau_D}+1\right)\left(\frac{\tau}{\gamma^2\tau_D}+1\right)^{0.5}}\right] \tag{7}$$

where A is a constant (≈ 0), γ is the axial-to-radial ratio of the dimension of the detection volume, which is estimated to be 4, N is the average number of molecules in the focal volume, τ_D is the diffusion time and τ is the time. τ_D can then be related to diffusion coefficient of NR dye in the bulk solution, D_b, by equation (8). where w_{xy}^2 is the calculated by using a solution with known diffusion coefficient.

$$\tau_D = \frac{w_{xy}^2}{4D_b} \tag{8}$$

In Figure 4.1, the blue line represents the fit of equation (7) to the data denoted by the red line, and the black dash lines represent the 95% confidence intervals.

The data were fit across the range of 10^{-6} to 10 seconds. The initial decay happening at few microseconds timescale is due to blinking which is beyond the scope of this study.

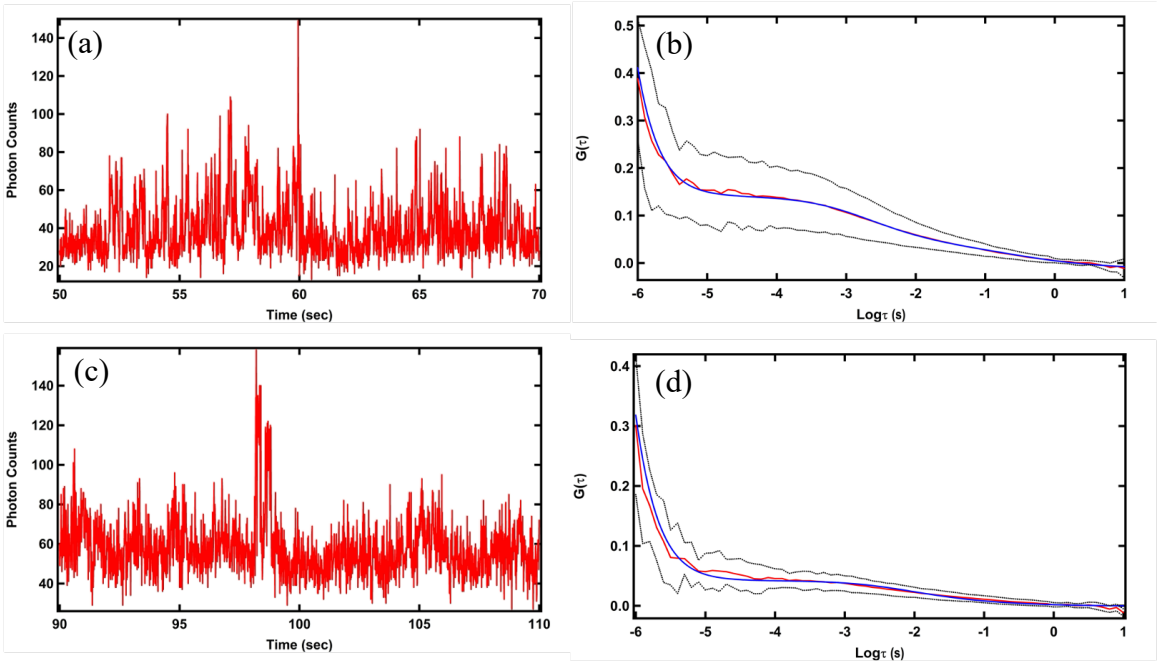

Figure 4.2 (a , b) photons intensity series alongside its autocorrelation decay plot of NR in ethanol solvent-filled 10nm nanopores, and (c, d) photons intensity series alongside its autocorrelation decay plot of NR in toluene solvent-filled 10nm nanopores. The red line represents the autocorrelation function, the blue line represents the fitted model. The dash black line represents the 95% confidence interval.

The second decay that happens in 10^{-4} timescale is caused by diffusion of NR molecules in and out of detection area. Comparing Figures 4.1b and 4.1d indicates that the NR in the bulk toluene gives a more rapid decay than that in the bulk ethanol. The data plotted in Figure 4.1b yielded a bulk diffusion D_b = 521 $\mu m^2/s$ for NR in bulk ethanol solution, while in Figure 4.1d shows the autocorrelation plot for the NR in bulk solution of toluene. We found a bulk diffusion coefficient for NR in toluene D_b = 842 $\mu m^2/s$ which is relatively faster compared to ethanol. This difference

arises due to the viscosity of ethanol being 1.8 times higher, which plays a role in the motions of dye molecules.

In the 10 and 20nm AAO membrane, we found 1D diffusion, resulting in slower autocorrelation decays. The photon intensity fluctuation and the decays observed from the 10 nm nanopores (Figure 4.2) were indeed slower, aligning with expectations of slower motion in nano pores. The autocorrelation data measured within the 10nm AAO membrane were found to be well characterized by a 1D two-component equation (9) with slower autocorrelation decays aligning with the expectations of transport hindrance. These components are described here as one-dimensional fast D_f and slow D_s diffusion.

$$G(\tau) = A + \frac{B_f}{\left(1+(\frac{\tau}{\gamma^2\tau_{Df}})\right)^{0.5}} + \frac{B_s}{\left(1+(\frac{\tau}{\gamma^2\tau_{Ds}})\right)^{0.5}} \quad (9)$$

In equation (9), A is a constant (≈ 0), B_f and B_s are amplitude of fast and slow diffusion, respectively, γ is the axial ratio of the focus, which is estimated to be 4, τ_{Df} is the diffusion time for D_f, τ_{Ds} is the diffusion time for D_s, τ_D is the diffusion time for initial decay and τ is the time.

Figures 4.2b and 4.2d show the fit of equation (9) to the autocorrelation decay for the ethanol and toluene-filled 10 nm AAO membranes with 95% confidence intervals. For the fitting purposes, we used the range from 10^{-6} to 10s. We found fast diffusion coefficient D_f = 210 $\mu m^2/s$ and slow diffusion coefficient D_s = 2.4 $\mu m^2/s$ for the NR in the ethanol-filled 10nm AAO membranes, while D_f = 89 $\mu m^2/s$ and D_s = 0.21 $\mu m^2/s$ in toluene-filled ones (see Table A.1 in the additional information). For the 10nm AAO membranes we found diffusion coefficients in nano pores filled by toluene smaller than those filled by ethanol, while the bulk diffusion coefficient in toluene greater than that in ethanol. This clearly indicates that the diffusion process in nano pores

is not governed by Stokes-Einstein's equation, other factors such as surface interactions of dye, also play a role.

The D_f and D_s values in the 10nm AAO membrane filled by ethanol were nearly 2.9 and 289 times less than the D_b in bulk ethanol. The significant difference between the D_s and D_b suggests a substantial hindrance to diffusion within the nanopores. For the toluene, however, the differences between the diffusion coefficients in the membrane and bulk diffusion coefficient are more substantial.

More specifically, we found the D_f and D_s values in the 10nm AAO membrane filled by toluene 9 and 10000 times less than the D_b value. The significant difference the D_s and D_b values indicate a considerable decrease in slow diffusion of molecules within the nanopores compared to the bulk medium (free diffusion). The observed variations in D_f and D_s values stem from the differing origins of these diffusion processes. D_f primarily arises from the less hindered diffusion of dye molecules through the nanopore, whereas D_s originates from dye molecules absorbed onto the pore surface before desorbing and passing through the membrane.

Results for the 20nm AAO membranes are presented in Figure 4.3. In the 20nm AAO membrane diffusion mechanism was quite different and the best model that fit the autocorrelation function was 1D one-component (equation 10), resulting in a faster autocorrelation decay of fast diffusion only. This makes sense as the pore sizes increases there are fewer collision with the pore surface thereby making dye diffusion more rapid just like in bulk solution.

$$G(\tau) = A + \frac{B_f}{\left(1+\left(\frac{\tau}{\gamma^2 \tau_{Df}}\right)\right)^{0.5}} \tag{10}$$

In equation 10, A is a constant (≈ 0), B_f is amplitude of fast diffusion respectively, γ is the axial ratio of the focus, τ_{Df} is the diffusion time for D_f , τ_D is the diffusion time for initial decay and τ is the time.

By fitting equation 10 to the autocorrelation data, we found D_f = 301 $\mu m^2/s$ for the ethanol and 143 $\mu m^2/s$ for the toluene-filled AAO membranes (see Table A.1). We found that the D_f value was approximately 1.7 and 5.7 times less than the bulk diffusion coefficient in the ethanol- and toluene-filled AAO membranes, respectively. Interestingly, there was no recorded D_s value for these larger nanopores. This suggests that as the pore size increases, there is less hindrance in the diffusion of NR dyes, possibly due to diminished confinement effects allowing for more unhindered movement of dye molecules.

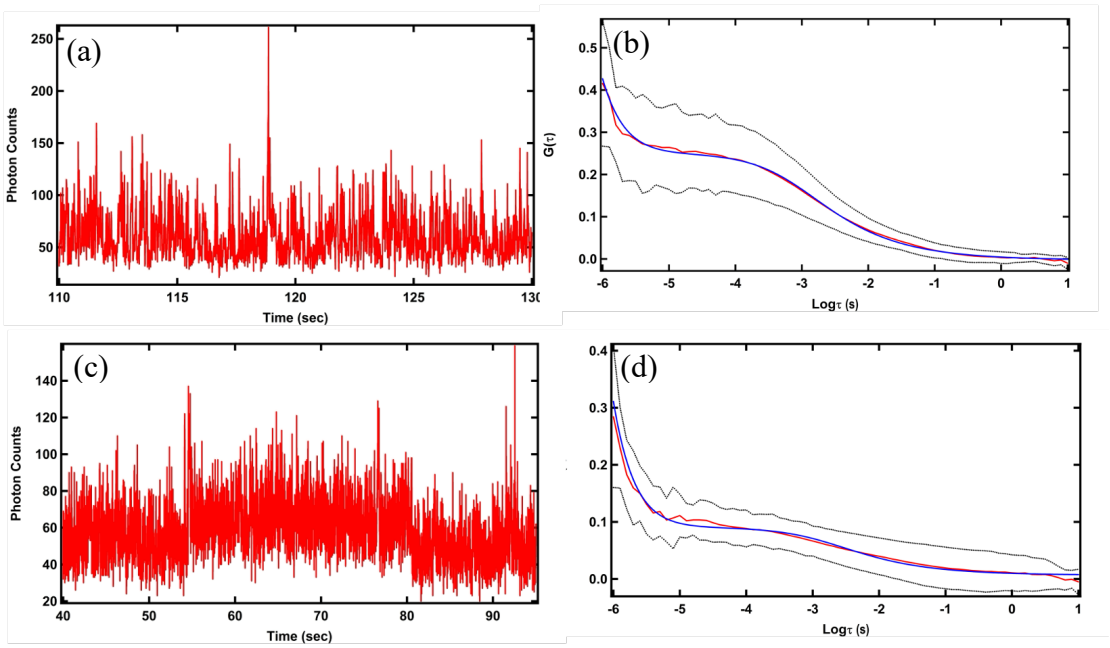

Figure 4.3 (a , b) photons intensity series alongside its autocorrelation decay plot of NR in ethanol solvent-filled 20nm nanopores, and (c, d) photons intensity series alongside its autocorrelation decay plot of NR in toluene solvent-filled 20nm nanopores. The red line represents the autocorrelation function, the blue line represents the fitted model. The dash black line represents the 95% confidence interval.

4.3 Multifractal Detrended Fluctuation Analysis

We first present the results of the sensitivity analysis on the randomly generated photon intensity series using the MF-DFA. Results presented in Figure 4.4 show the generalized Hurst exponent, $h(q)$, against the moment, q, for three series of length N_s = 1,500,000 (Fig. 4.4a), 150,000 (Figure. 4.4b), and 15,000 (Figure. 4.4c). Smaller q values on these plots correspond to higher frequency events, and larger values to lower frequency events. Each data point in this figure represents the average over 100 realizations. Theoretically, one should expect $H = h(q = 2) = 0.5$ for stationary and uncorrelated random series e.g., white noises. (Kantelhardt et al., 2002a) For the randomly generated photon intensity series with time bins 0.1, 1 and 10ms respectively we found $H = h(q = 2) = 0.50$, 0.50 and 0.53 for the original series, and $H = h(q = 2) = 0.50$, 0.51 and 0.51 for the shuffled series, and $H = h(q = 2) = 0.51$, 0.50 and 0.53 for the surrogated series (see Table A.2 in the additional information). As shown in Figure 4.4, we found $h(q)$ is almost constant and near 0.5 for all generated series, similar to random walk series. We also found that the MF-DFA results were impacted by the length of the series. More specifically, the shorter the series length become (from top to bottom in Figure 3.1), the more uncertain the results of MF-DFA would be. Nonetheless, generally, the value of $h(q)$ is near 0.5, and the results of the MF-DFA are reasonable.

In Figures 4.4a and 4.4b, the results of the MF-DFA for the original, shuffle and surrogate series are very close to each other. However, in Figure 4.4c slight deviations are observed indicating the effect of series length. Kantelhardt et al. (2002) also indicated that the accuracy of $h(q)$ calculated via the MF-DFA depended on the length of a series.

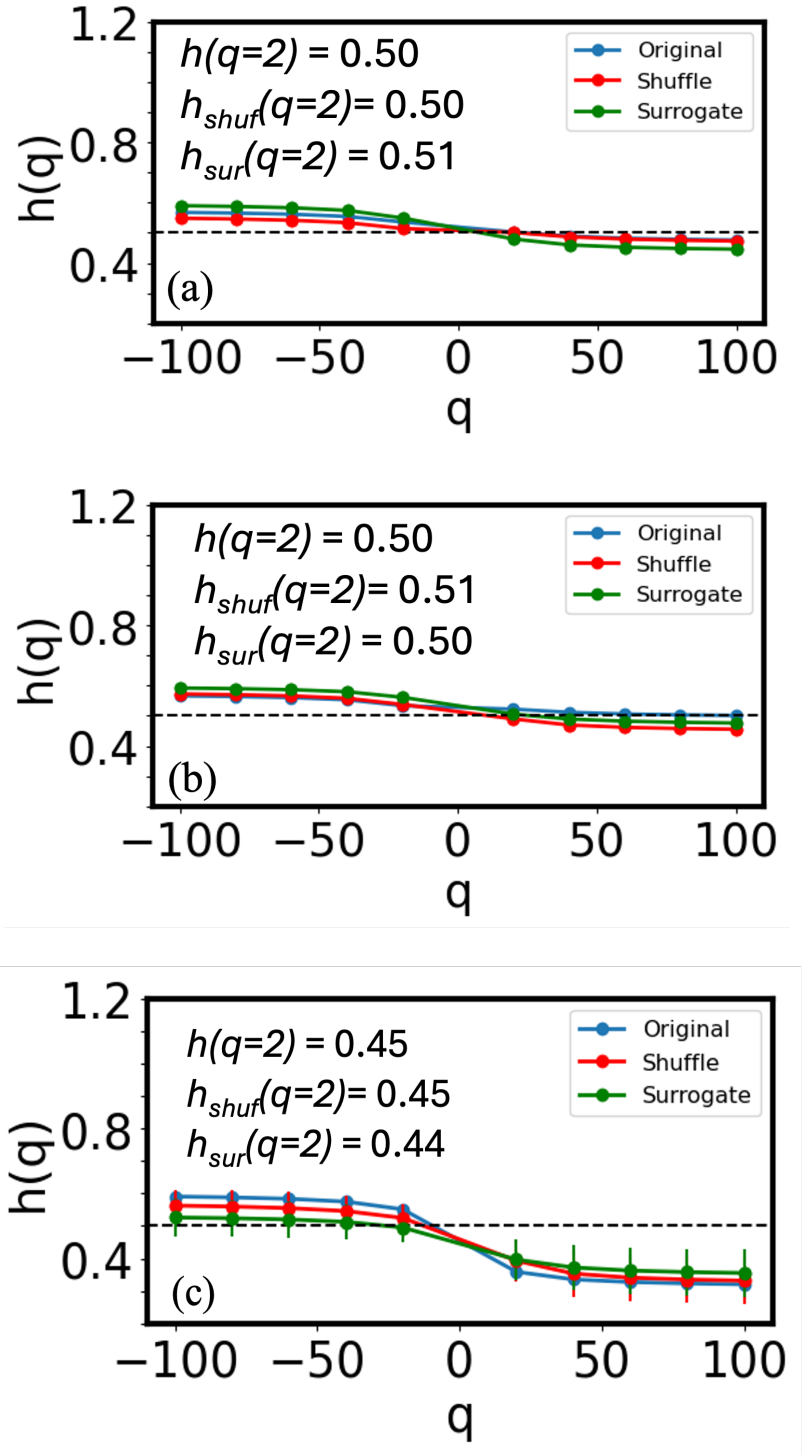

Figure 4.4 The generalized Hurst exponent, h(q), versus the order q for randomly generated series of length N_S = (a) 1,500,000, (b) 150,000, and (c) 15,000. From top to bottom deviations from 0.5 becomes more significant demonstrating the effect of series length on the MF-DFA results. The black dash line represents 0.5 benchmark.

More specifically, they reported that for $q = \pm 10$ one should expect errors in $h(q)$ as large as ± 0.1 and ± 0.05 for series of length N_s = 10,000 and 100,000, respectively, consistent with our results shown in Figures 4.4b and 4.4c.

Figures 4.5 and 4.6 shows the results of the MF-DFA for the photon intensity series and the NR in the bulk solution of ethanol and toluene respectively. In these Figures, the results are presented for three time bins (0.1, 1 and 10ms). As can be seen, for both ethanol and toluene, although the moment q varies over a wide range from -100 to +100, the generalized Hurst exponent $h(q)$ is near 0.5 for the 0.1ms time bin with N_s = 1,500,000 (Figures 4.5a and 4.6a). The original, shuffle and surrogate results are also very similar. For the lower frequency photon counts ($0 \leq q \leq 100$), we found $h(q)$ slightly less than 0.5, while for the higher frequency photon counts ($-100 \leq q \leq 0$), its value is slightly greater than 0.5, similar to the results presented in Figure 4.4.

We also observed similar results for time bins 1ms (Figures 4.5b and 4.5c) and 10ms (Figures 4.6b and 4.6c). However, deviations from $h(q)$ = 0.5 becomes more obvious from top (time bin 0.1ms) to bottom (time bin 10ms). As stated earlier, similar to the results of Kantelhardt et al. (2012) one should expect errors in the $h(q)$ calculation when the length of series becomes shorter. The value of $h(q) \approx 0.5$ in Figure 5 indicates Brownian noise. It is also consistent with the expected Fickian diffusion in bulk solution. For stationary series the Hurst exponent $H = h(q = 2)$, (Sadegh Movahed & Hermanis, 2008) and $H = 0.5$ corresponds to the classical Brownian motion (Feder, 1991).

Figures 4.7 and 4.8 display the MF-DFA results for the 10nm AAO membrane filled by the solvent ethanol and toluene.

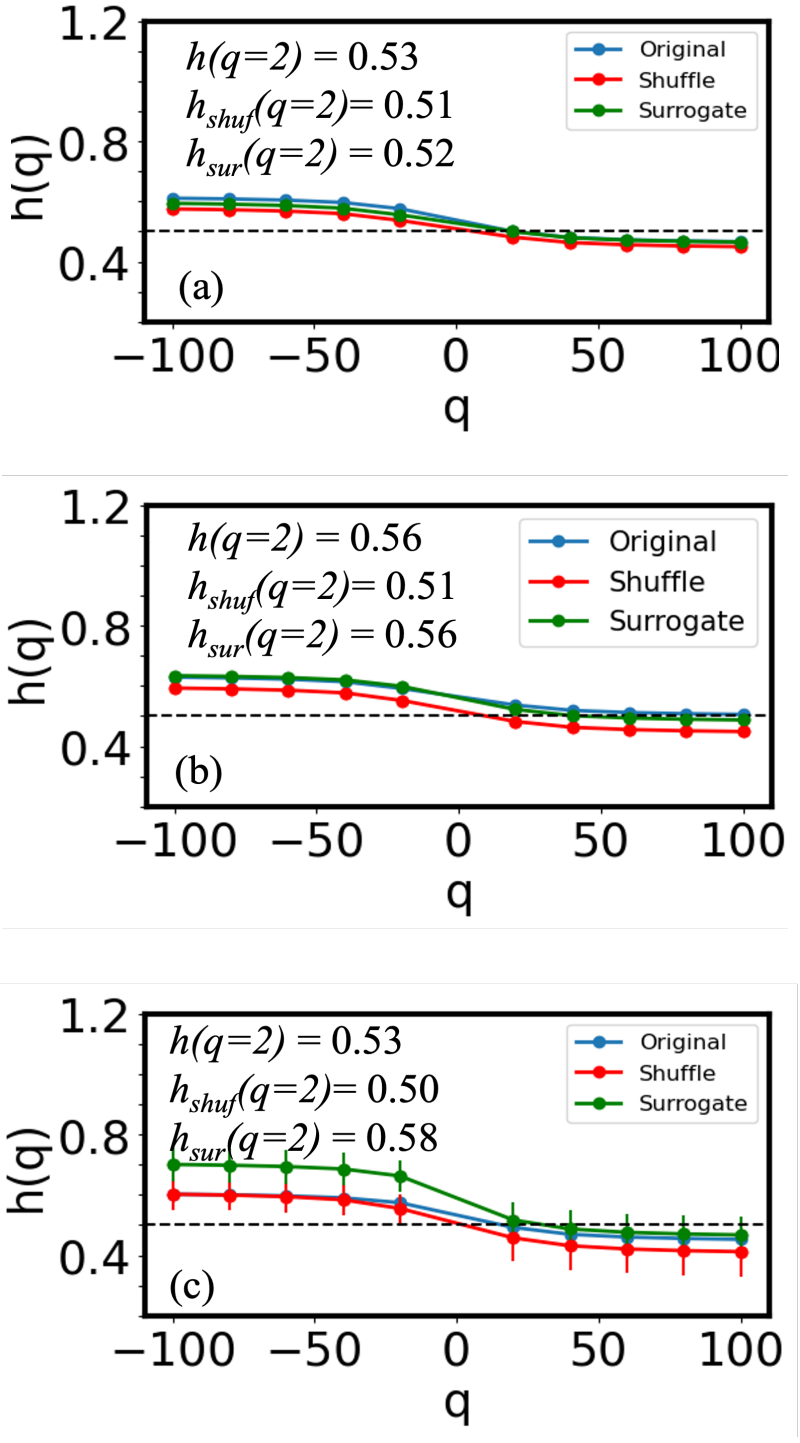

Figure 4.5 The generalized Hurst exponent, $h(q)$, as a function of the moment, , q, for the (a) 0.1ms, (b) 1ms, (c) 10mn time bins of the NR in the ethanol solution. The blue, red and green curves represent respectively the original, shuffle and surrogate results. The black dash line represents $h(q)$ benchmark.

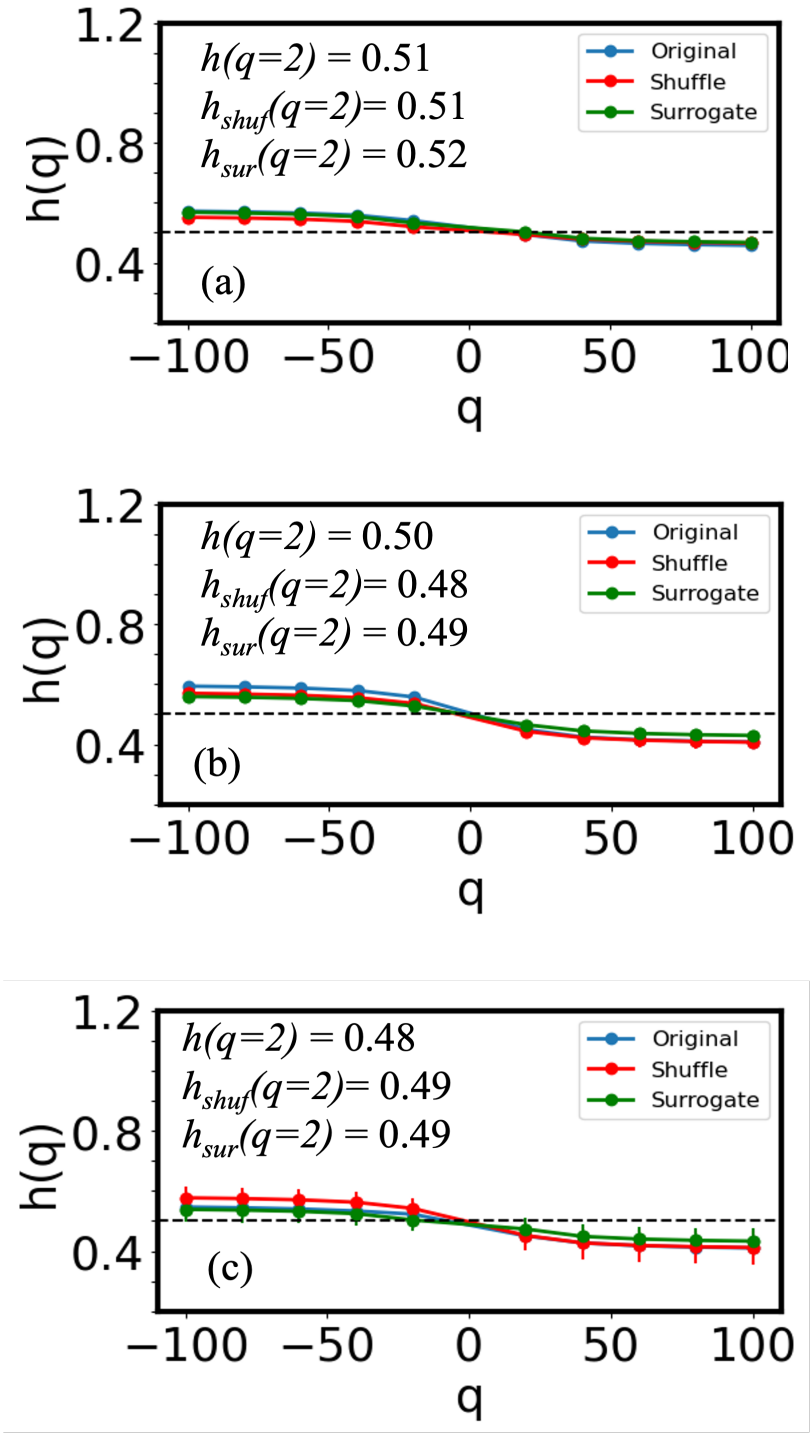

Figure 4.6 The generalized Hurst exponent, $h(q)$, as a function of the moment, , q, for the (a) 0.1ms, (b) 1ms, (c) 10mn time bins of the NR in the toluene solution. The blue, red and green curves represent respectively the original, shuffle and surrogate results. The black dash line represents $h(q)$ benchmark.

Results for the 20nm AAO membrane are given in Figures 4.9 and 4.10. Each data point represents the average over seven experiments, and each error bar denotes one standard deviation. For the original series and ethanol solvent-filled 10nm AAO membrane, we found $0.64 \leq h(q) \leq 0.82$ for time bin 0.1ms, $0.70 \leq h(q) \leq 0.84$ for time bin 1ms and $0.72 \leq h(q) \leq 1.06$ for time bin 10ms. Compared to the MF-DFA results in ethanol and toluene bulk solutions shown in Figures 4.5 and 4.6, we found stronger multifractality for the solvents in 10 and 20nm AAO membranes (Figures 4.7 to 4.10). For the ethanol-solvent filled 10nm AAO membrane, the Hurst exponent $H = h(q = 2)$ was 0.73, 0.77 and 0.88 for time bins 0.1, 1 and 10ms, respectively, for the original series (Table A3). For the toluene solvent-filled 10nm AAO membrane, the H was 0.73, 0.72 and 0.78 (Table A3). Recall that $0.5 < H < 1$ corresponds to persistence (positive correlation). The $h(q = 2) > 0.5$ corresponds to super diffusion (Metzler & Klafter, 2004; Sliusarenko et al., 2010; Telesca et al., 2018). Telesca et al. (2018) recently analyzed intensity time series of photons scattered by tracer particles in a polymeric gel and reported anomalous diffusion (sub or super diffusion). In their study, they found the Hurst exponent $H < 0.5$ (antipersistence) and deduced that dynamics of tracers in a polymetric gel to be sub-diffusive, and $H > 0.5$ super diffusion in agreement with their mean square displacement-time data. The H values reported in (Table A.3), clearly demonstrate that the diffusion in the 10 and 20nm AAO membranes were super diffusion. As can be seen from Figures 4.7 to 4.10, after shuffling the photon intensity series measured in 10 and 20nm AAO membranes, the $h(q)$ values dropped down to near 0.5, while the $h(q)$ values for the surrogated series did not change compared to the values for the original series. This means the source of multifractality is mainly due to long-range correlations in the photon intensity time series. Results presented in Figures 4.7 to 4.10 also show that long-range correlations in the photon

intensity series existed for both lower and higher frequency events corresponding to $0 < q < 100$ and $-100 < q < 0$, respectively.

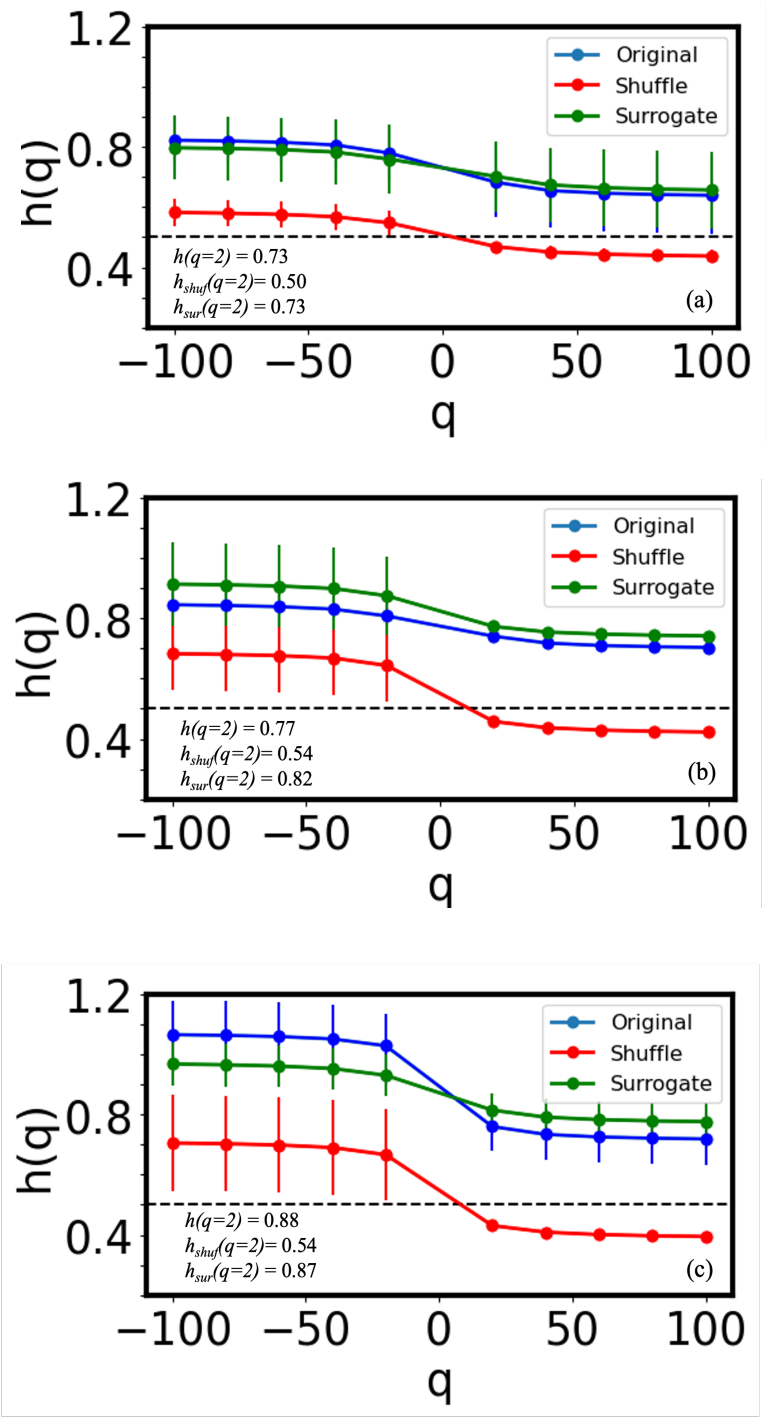

Figure 4.7 The generalized Hurst exponent, $h(q)$, as a function of the moment, q, for (a) 0.1ms, (b) 1ms, (c) 10mn time bins of the NR in the ethanol filled 10nm membrane. The blue,

red and green curves represent respectively the original, shuffle and surrogate results. The black dash line represents $h(q)$ benchmark.

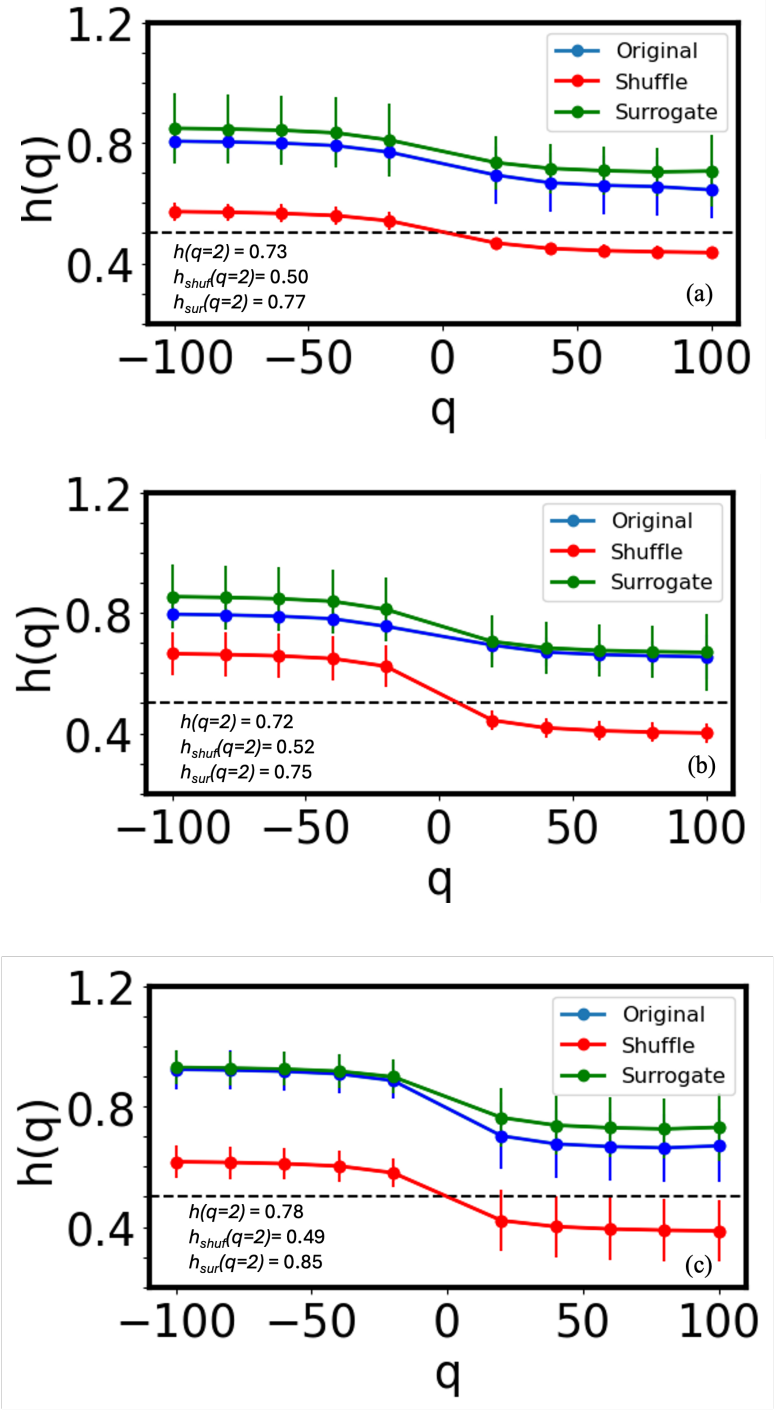

Figure 4.8 The generalized Hurst exponent, $h(q)$, as a function of the moment, q, for (a) 0.1ms, (b) 1ms, (c) 10mn time bins of the NR in the toluene filled 10nm membrane. The blue,

red and green curves represent respectively the original, shuffle and surrogate results. The black dash line represents $h(q)$ benchmark.

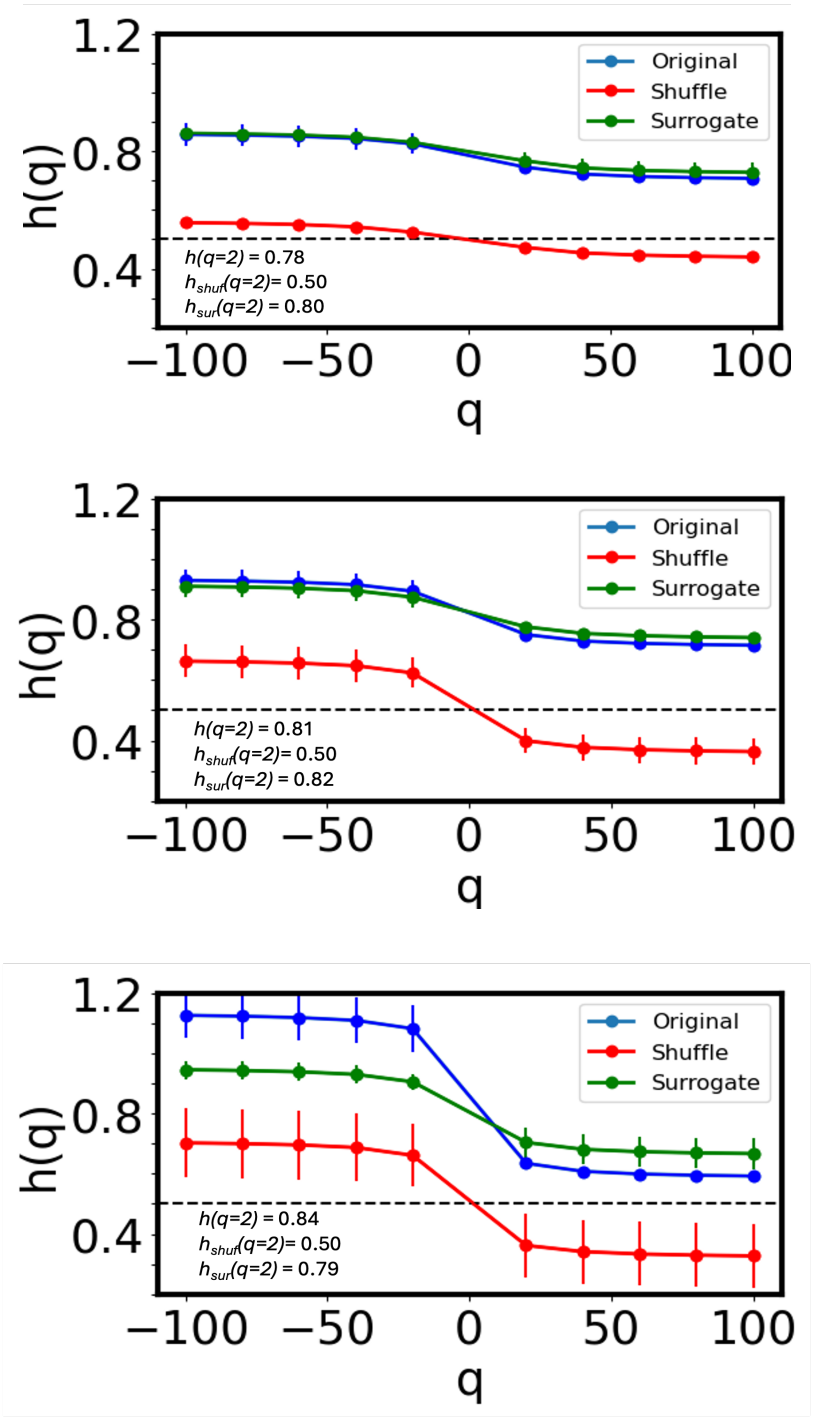

Figure 4.9 The generalized Hurst exponent, $h(q)$, as a function of the moment, q, for 0.1ms time bins top image, 1ms time bins middle and bottom 10mn time bins of the NR in the ethanol filled 20nm membrane. The blue, red and green curves represent respectively the original, shuffle and surrogate results. The black dash line represents $h(q)$ benchmark.

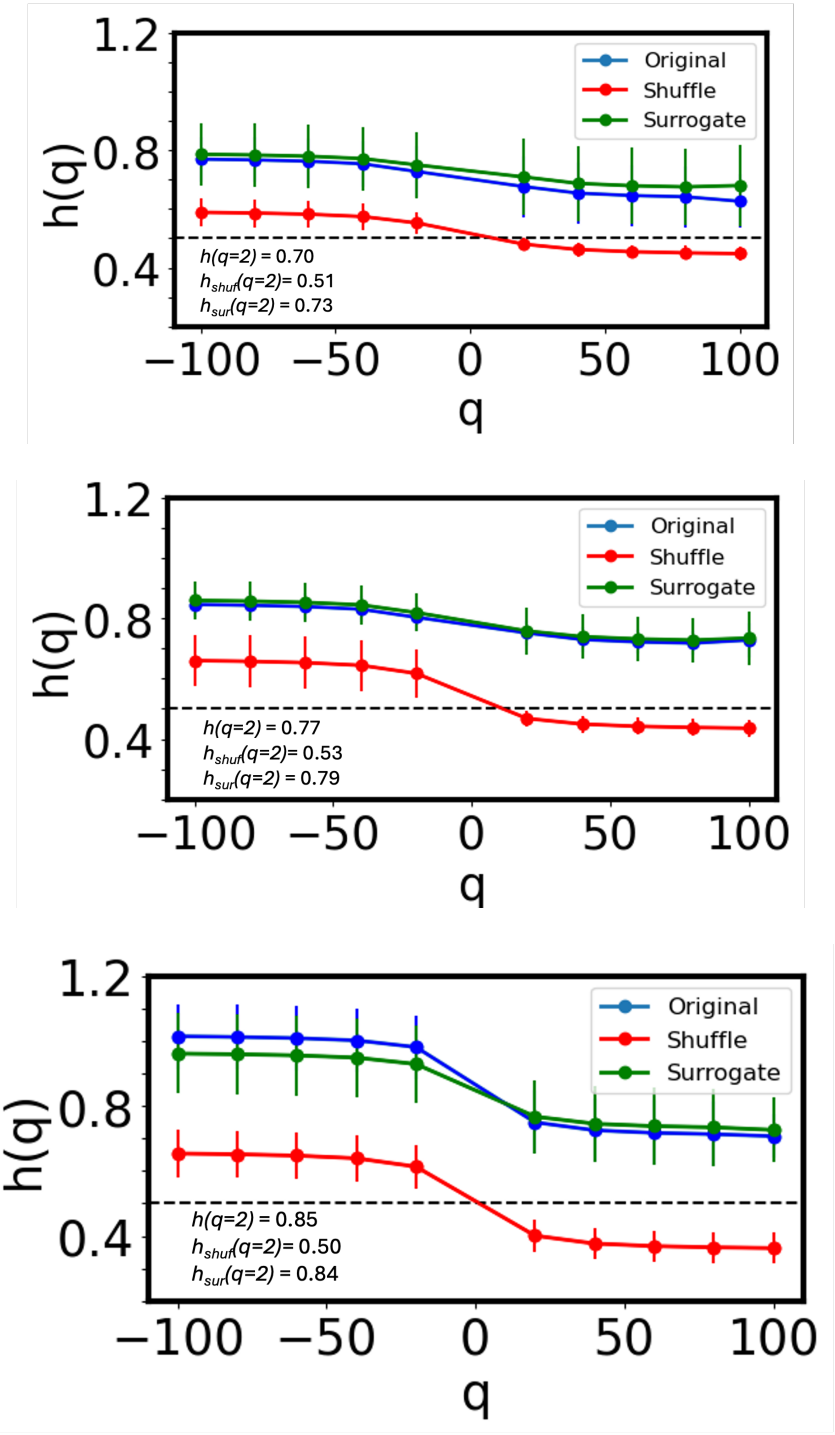

Figure 4.10 The generalized Hurst exponent, $h(q)$, as a function of the moment, q, for 0.1ms time bins top image, 1ms time bins middle and bottom 10mn time bins of the NR in the toluene filled 20nm membrane. The blue, red and green curves represent respectively the original, shuffle and surrogate results. The black dash line represents $h(q)$ benchmark.

Chapter 5 - Conclusion

In this study, we employed fluorescence correlation spectroscopy (FCS) method in combination with multifractal detrended fluctuation analysis (MF-DFA) to investigate the rate and mechanisms of Nile Red (NR) diffusion in bulk solutions, 10 and 20nm AAO nanostructured membranes filled with pure ethanol or toluene solutions. Our FCS findings unveiled a dual-component diffusion mechanism for the NR within 10nm and 20nm toluene-filled nanopores, characterized by fast (D_f) and slow (D_s) diffusion, while one component of diffusion mechanism (D_f) within the 20nm ethanol-filled nanopores. These processes exhibited significantly smaller diffusion coefficients, D_f and D_s, compared to the bulk NR diffusion coefficient, D_b, measured in the bulk solutions. Also, we observed an increase in diffusion rate with an increase in pore size.

Results of the MF-DFA revealed that the generalized Hurst exponent $h(q = 2)$ was near 0.5 for the bulk solutions in accord with the classical Brownian motion and Fickian diffusion. For both 10 and 20nm AAO membranes, however, $h(q = 2)$ was found to be greater than 0.5 consistent with super diffusion. Application of the MF-DFA techniques on photon time series provided further evidence essential for enhancing the characterization of molecular transport mechanisms within nanoporous media that are not accessible through FCS.

Lastly, further investigations are still required to measure mean squared displacement as a function of time by tracking molecules in the same membranes and double check with our calculated $h(q = 2)$.

References

Alam, A., Wang, N., Petraki, E., Barkat, A., Huang, F., Shah, M. A., Cantzos, D., Priniotakis, G., Yannakopoulos, P. H., Papoutsidakis, M., & Nikolopoulos, D. (2021). Fluctuation Dynamics of Radon in Groundwater Prior to the Gansu Earthquake, China (22 July 2013: M s = 6.6): Investigation with DFA and MFDFA Methods. *Pure and Applied Geophysics*, *178*(9), 3375–3395. https://doi.org/10.1007/s00024-021-02818-8

Brooks Shera, E., Seitzinger, N. K., Davis, L. M., Keller, R. A., & Soper, S. A. (1990). Detection of single fluorescent molecules. *Chemical Physics Letters*, *174*(6), 553–557. https://doi.org/10.1016/0009-2614(90)85485-U

Castez, M. F., Winograd, E. A., & Sánchez, V. M. (2017). Methane Flow through Organic-Rich Nanopores: The Key Role of Atomic-Scale Roughness. *Journal of Physical Chemistry C*, *121*(51), 28527–28536. https://doi.org/10.1021/ACS.JPCC.7B09811/ASSET/IMAGES/JP-2017-09811R_M008.GIF

Chen, H., Sun, X., Chen, H., Wu, Z., & Wang, B. (2004). Some problems in multifractal spectrum computation using a statistical method. *New Journal of Physics*, *6*(1), 84. https://doi.org/10.1088/1367-2630/6/1/084

Cho, H. J., Sigmund, E. E., & Song, Y. (2012). Magnetic Resonance Characterization of Porous Media Using Diffusion through Internal Magnetic Fields. *Materials 2012, Vol. 5, Pages 590-616*, *5*(4), 590–616. https://doi.org/10.3390/MA5040590

Cussler, E. L. (1997). Diffusion: Mass Transfer in Fluid Systems, 2nd edition. *Cambridge University Press*, 600.

Drożdż, S., Minati, L., Oświęcimka, P., Stanuszek, M., & Wątorek, M. (2019). Signatures of the Crypto-Currency Market Decoupling from the Forex. *Future Internet*, *11*(7), 154. https://doi.org/10.3390/fi11070154

Dutta, S., Ghosh, D., & Chatterjee, S. (2013). Multifractal detrended fluctuation analysis of human gait diseases. *Frontiers in Physiology*, *4 OCT*. https://doi.org/10.3389/fphys.2013.00274

Eigen, M., & Rigler, R. (1994). Sorting single molecules: application to diagnostics and evolutionary biotechnology. *Proceedings of the National Academy of Sciences*, *91*(13), 5740–5747. https://doi.org/10.1073/PNAS.91.13.5740

Elson, E. L., & Magde, D. (1974). Fluorescence correlation spectroscopy. I. Conceptual basis and theory. *Biopolymers*, *13*(1), 1–27. https://doi.org/10.1002/BIP.1974.360130102

Fang, T., Wang, M., Wang, C., Liu, B., Shen, Y., Dai, C., & Zhang, J. (2017). Oil detachment mechanism in CO2 flooding from silica surface: Molecular dynamics simulation. *Chemical Engineering Science*, *164*, 17–22. https://doi.org/10.1016/J.CES.2017.01.067

Feder, J. (1991). Fractal Time-Series and Fractional Brownian Motion. *Riste, T., Sherrington, D. (Eds) Spontaneous Formation of Space-Time Structures and Criticality. NATO ASI Series, Vol 349. Springer, Dordrecht.* .

Ghanbarian, B., Liang, F., … H. L. U. R., & 2023, undefined. (n.d.). Unconventional Reservoirs. *Books.Google.ComB Ghanbarian, F Liang, HH LiuPhysics of Fluid Flow and Transport in Unconventional Reservoir Rocks, 2023•books.Google.Com*. Retrieved March 13, 2024, from https://books.google.com/books?hl=en&lr=&id=J6i5EAAAQBAJ&oi=fnd&pg=RA1-PA5&dq=Physics+of+Fluid+Flow+and+Transport+in+Unconventional+Reservoir+by+Ghanbarian&ots=HlNZbV1oDZ&sig=JNr3bxfxcDL53eJ30j2wAuO49_s

Hakso, A., & Zoback, M. (2019). The relation between stimulated shear fractures and production in the Barnett Shale: Implications for unconventional oil and gas reservoirs. *Geophysics*, *84*(6), B461–B469. https://doi.org/10.1190/GEO2018-0545.1

He, J., Ju, Y., Lammers, L., Kulasinski, K., & Zheng, L. (2020). Tortuosity of kerogen pore structure to gas diffusion at molecular- and nano-scales: A molecular dynamics simulation. *Chemical Engineering Science*, *215*, 115460. https://doi.org/10.1016/J.CES.2019.115460

Higgins, D. A., Park, S. C., Tran-Ba, K. H., & Ito, T. (2015). Single-Molecule Investigations of Morphology and Mass Transport Dynamics in Nanostructured Materials. *Https://Doi.Org/10.1146/Annurev-Anchem-071114-040153*, *8*, 193–216. https://doi.org/10.1146/ANNUREV-ANCHEM-071114-040153

Hohlbein, J., Steinhart, M., Schiene-Fischer, C., Benda, A., Hof, M., & Hübner, C. G. (2007). Confined diffusion in ordered nanoporous alumina membranes. *Small*, *3*(3), 380–385. https://doi.org/10.1002/SMLL.200600398

Huang, L., Ning, Z., Wang, Q., Qi, R., Zeng, Y., Qin, H., Ye, H., & Zhang, W. (2018). Molecular simulation of adsorption behaviors of methane, carbon dioxide and their mixtures on kerogen: Effect of kerogen maturity and moisture content. *Fuel*, *211*, 159–172. https://doi.org/10.1016/J.FUEL.2017.09.060

Ihlen, E. A. F. (2012). Introduction to multifractal detrended fluctuation analysis in Matlab. *Frontiers in Physiology*, *3 JUN*. https://doi.org/10.3389/fphys.2012.00141

Ivanov, P. C., Nunes Amaral, L. A., Goldberger, A. L., Havlin, S., Rosenblum, M. G., Struzik, Z. R., & Stanley, H. E. (1999). Multifractality in human heartbeat dynamics. *Nature 1999 399:6735*, *399*(6735), 461–465. https://doi.org/10.1038/20924

Kantelhardt, J. W. (2012). Fractal and Multifractal Time Series. In *Mathematics of Complexity and Dynamical Systems* (pp. 463–487). Springer New York. https://doi.org/10.1007/978-1-4614-1806-1_30

Kantelhardt, J. W., Zschiegner, S. A., Koscielny-Bunde, E., Havlin, S., Bunde, A., & Stanley, H. E. (2002a). Multifractal detrended fluctuation analysis of nonstationary time series. *Physica A: Statistical Mechanics and Its Applications*, *316*(1–4), 87–114. https://doi.org/10.1016/S0378-4371(02)01383-3

Kantelhardt, J. W., Zschiegner, S. A., Koscielny-Bunde, E., Havlin, S., Bunde, A., & Stanley, H. E. (2002b). Multifractal detrended fluctuation analysis of nonstationary time series. *Physica A: Statistical Mechanics and Its Applications*, *316*(1–4), 87–114. https://doi.org/10.1016/S0378-4371(02)01383-3

Kärger, J., & Valiullin, R. (2013). Mass transfer in mesoporous materials: the benefit of microscopic diffusion measurement. *Chemical Society Reviews*, *42*(9), 4172–4197. https://doi.org/10.1039/C3CS35326E

Loucks, R. G., & Reed, R. M. (2014). *Scanning-Electron-Microscope Petrographic Evidence for Distinguishing Organic-Matter Pores Associated with Depositional Organic Matter versus Migrated Organic Matter in Mudrock*. www.gcags.org

Loucks, R. G., Reed, R. M., Ruppel, S. C., & Hammes, U. (2012). Spectrum of pore types and networks in mudrocks and a descriptive classification for matrix-related mudrock pores. *AAPG Bulletin*, *96*(6), 1071–1098. https://doi.org/10.1306/08171111061

Madanchi, A., Taghavi-Shahri, F., Taghavi-Shahri, S. M., & Rahimi Tabar, M. R. (2020). Scaling behavior in measured keystroke time series from patients with Parkinson's disease. *European Physical Journal B*, *93*(7). https://doi.org/10.1140/epjb/e2020-100561-4

Magde, D., Elson, E., & Webb, W. W. (1972). Thermodynamic fluctuations in a reacting system measurement by fluorescence correlation spectroscopy. *Physical Review Letters*, *29*(11), 705–708. https://doi.org/10.1103/PHYSREVLETT.29.705

Mahale, V. P., Chakraborty, B., Rao, V. P., & Salkar, T. (2022). Characterization of carbonate platform bathymetry off western India employing multifractal detrended fluctuation analysis (MFDFA). *Oceans Conference Record (IEEE)*. https://doi.org/10.1109/OCEANSChennai45887.2022.9775483

Metzler, R., & Klafter, J. (2004). The restaurant at the end of the random walk: recent developments in the description of anomalous transport by fractional dynamics. *Journal of Physics A: Mathematical and General*, *37*(31), R161. https://doi.org/10.1088/0305-4470/37/31/R01

Moerner, W. E., & Kador, L. (1989). Optical detection and spectroscopy of single molecules in a solid. *Physical Review Letters*, *62*(21), 2535–2538. https://doi.org/10.1103/PHYSREVLETT.62.2535/FIGURE/1/THUMB

Morales Martínez, J. L., Segovia-Domínguez, I., Rodríguez, I. Q., Horta-Rangel, F. A., & Sosa-Gómez, G. (2021). A modified Multifractal Detrended Fluctuation Analysis (MFDFA) approach for multifractal analysis of precipitation. *Physica A: Statistical Mechanics and Its Applications*, *565*. https://doi.org/10.1016/j.physa.2020.125611

Movahed, M. S., Jafari, G. R., Ghasemi, F., Rahvar, S., & Tabar, M. R. R. (2006). Multifractal detrended fluctuation analysis of sunspot time series. *Journal of Statistical Mechanics: Theory and Experiment*, *2*. https://doi.org/10.1088/1742-5468/2006/02/P02003

Orrit, M., & Bernard, J. (1990). Single pentacene molecules detected by fluorescence excitation in a *p*-terphenyl crystal. *Physical Review Letters*, *65*(21), 2716. https://doi.org/10.1103/PhysRevLett.65.2716

Pavlov, A. N., Abdurashitov, A. S., Koronovskii, A. A., Pavlova, O. N., Semyachkina-Glushkovskaya, O. V., & Kurths, J. (2020). Detrended fluctuation analysis of cerebrovascular responses to abrupt changes in peripheral arterial pressure in rats. *Communications in Nonlinear Science and Numerical Simulation*, *85*. https://doi.org/10.1016/j.cnsns.2020.105232

Pedron, I. T. (2010). Correlation and multifractality in climatological time series. *Journal of Physics: Conference Series*, *246*. https://doi.org/10.1088/1742-6596/246/1/012034

Peng, C.-K., Buldyrev, S. V, Havtin, S., Simons, M., Stanley, H. E., & Goldbergerz, A. L. (1994). Mosaic organization of DNA nucleotides. *PHYSICAL REVIEW E*, *49*(2).

Rashidi, H., Howard, K. J., Ito, T., & Higgins, D. A. (2023). Random Walks and Sticky Surfaces: Single-Molecule Measurements of Solute Diffusion in Ethanol/Water-Filled Anodic Alumina Nanopores. *Journal of Physical Chemistry C*, *127*(1), 411–420. https://doi.org/10.1021/ACS.JPCC.2C07083/ASSET/IMAGES/LARGE/JP2C07083_0008.JPEG

Sadegh Movahed, M., & Hermanis, E. (2008). Fractal analysis of river flow fluctuations. *Physica A: Statistical Mechanics and Its Applications*, *387*(4), 915–932. https://doi.org/10.1016/J.PHYSA.2007.10.007

Shadkhoo, S., Ghanbarnejad, F., Jafari, G. R., & Tabar, M. R. R. (2009). Scaling behavior of earthquakes' inter-events time series. *Central European Journal of Physics*, *7*(3), 620–623. https://doi.org/10.2478/s11534-009-0058-0

Sliusarenko, O. Y., Gonchar, V. Y., Chechkin, A. V., Sokolov, I. M., & Metzler, R. (2010). Kramers-like escape driven by fractional Gaussian noise. *Physical Review E - Statistical, Nonlinear, and Soft Matter Physics*, *81*(4), 041119. https://doi.org/10.1103/PHYSREVE.81.041119/FIGURES/16/MEDIUM

Subhakar, D., & Chandrasekhar, E. (2016). Reservoir characterization using multifractal detrended fluctuation analysis of geophysical well-log data. *Physica A: Statistical Mechanics and Its Applications*, *445*, 57–65. https://doi.org/10.1016/j.physa.2015.10.103

Takahara, S., Kittaka, S., Mori, T., Kuroda, Y., Takamuku, T., & Yamaguchi, T. (2008). Neutron scattering and dielectric studies on dynamics of methanol and ethanol confined in MCM-41. *Journal of Physical Chemistry C*, *112*(37), 14385–14393. https://doi.org/10.1021/JP8015062/ASSET/IMAGES/LARGE/JP-2008-015062_0003.JPEG

Telesca, L., Haro-Pérez, C., Moreno-Torres, R., & Ramirez-Rojas, A. (2018). Multifractal detrended fluctuation analysis of intensity time series of photons scattered by tracer particles within a polymeric gel. *Physica A*, *490*, 994–1003. https://doi.org/10.1016/j.physa.2017.08.080

Telesca, L., Lapenna, V., & MacChiato, M. (2005). Multifractal fluctuations in seismic interspike series. *Physica A: Statistical Mechanics and Its Applications*, *354*(1–4), 629–640. https://doi.org/10.1016/j.physa.2005.02.053

Tessier, Y., Lovejoy, S., Hubert, P., Schertzer, D., & Pecknold, S. (1996). Multifractal analysis and modeling of rainfall and river flows and scaling, causal transfer functions. *Journal of*

Geophysical Research Atmospheres, *101*(21), 26427–26440. https://doi.org/10.1029/96jd01799

Tran-Ba, K. H., Higgins, D. A., & Ito, T. (2015). Fluorescence recovery after photobleaching and single-molecule tracking measurements of anisotropic diffusion within identical regions of a cylinder-forming diblock copolymer film. *Analytical Chemistry*, *87*(11), 5802–5809. https://doi.org/10.1021/ACS.ANALCHEM.5B01041/SUPPL_FILE/AC5B01041_SI_007.AVI

Ungerer, P., Collell, J., & Yiannourakou, M. (2015). Molecular modeling of the volumetric and thermodynamic properties of kerogen: Influence of organic type and maturity. *Energy and Fuels*, *29*(1), 91–105. https://doi.org/10.1021/EF502154K/ASSET/IMAGES/LARGE/EF-2014-02154K_0015.JPEG

Vinh, N. Q., Allen, S. J., & Plaxco, K. W. (2011). Dielectric spectroscopy of proteins as a quantitative experimental test of computational models of their low-frequency harmonic motions. *Journal of the American Chemical Society*, *133*(23), 8942–8947. https://doi.org/10.1021/JA200566U/SUPPL_FILE/JA200566U_SI_001.PDF

Zhang, L., Liu, C., Liu, Y., Li, Q., Cheng, Q., & Cai, S. (2020). Transport Property of Methane and Ethane in K-Illite Nanopores of Shale: Insights from Molecular Dynamic Simulations. *Energy and Fuels*, *34*(2), 1710–1719. https://doi.org/10.1021/ACS.ENERGYFUELS.9B04255/ASSET/IMAGES/LARGE/EF9B04255_0001.JPEG

Appendix A - Additional Information.

Table A.1 Experimental diffusion coefficients obtained from the study

Solvent	Bulk solution		10nm AAO membrane				20nm AAO membrane			
	D_b ($\mu m^2/s$)	95% C.I.	D_f ($\mu m^2/s$)	95% C.I.	D_s ($\mu m^2/s$)	95% C.I.	D_f ($\mu m^2/s$)	95% C.I.	D_s ($\mu m^2/s$)	95% C.I
Ethanol	521	39	210	62	2.4	1.6	301	14	-	-
Toluene	842	157	89	34	0.21	0.16	240	110	0.13	0.272

Table A.2 The Hurst Exponent H calculated from $h(q=2)$ for randomly generated time series

	$H = h(q = 2)$			
Randomly generated series following Poisson distribution	Series	0.1ms	1ms	10ms
	Original	0.50	0.50	0.45
	Shuffle	0.50	0.51	0.45
	Surrogate	0.51	0.50	0.44

Table A.3 The Hurst Exponent *H* calculated from *h*(*q*=2) for the photon intensity series measured in ethanol and toluene bulk solutions as well as the ethanol and toluene solvent-filled 10 and 20nm AAO Membranes

		$H = h(q = 2)$					$H = h(q = 2)$		
	Series	0.1ms	1ms	10ms		Series	0.1ms	1ms	10ms
Ethanol Bulk Solution	Original	0.53	0.56	0.53	Toluene Bulk Solution	Original	0.51	0.50	0.48
	Shuffle	0.51	0.51	0.50		Shuffle	0.51	0.48	0.49
	Surrogate	0.52	0.56	0.58		Surrogate	0.52	0.49	0.49
Ethanol 10nm membrane	Original	0.73	0.77	0.88	Toluene 10nm membrane	Original	0.73	0.72	0.78
	Shuffle	0.50	0.54	0.54		Shuffle	0.50	0.52	0.49
	Surrogate	0.73	0.82	0.87		Surrogate	0.77	0.75	0.82
Ethanol 20nm membrane	Original	0.78	0.81	0.84	Toluene 20nm membrane	Original	0.70	0.77	0.85
	Shuffle	0.50	0.50	0.50		Shuffle	0.51	0.53	0.50
	Surrogate	0.80	0.82	0.79		Surrogate	0.73	0.79	0.84